pp Elastic Scattering at LHC in a Nucleon–Structure Model

M. M. Islam^{a,}, *J. Kašpar^{b} and R. J. Luddy^{c}*

^{a}Department of Physics, University of Connecticut, Storrs, CT 06269, USA, (islam@phys.uconn.edu)

^{b} TOTEM Collaboration, CERN, Geneva, Switzerland (Jan.Kaspar@cern.ch)

   Institute of Physics, Academy of Sciences of the Czech Republic, Prague

^{c} Department of Physics, University of Connecticut, Storrs, CT 06269, USA, (RJLuddy@phys.uconn.edu)

Abstract

We predict pp elastic differential cross sections at LHC at c.m. energy 14 TeV and momentum transfer range $|t| = 0 - 10$ GeV^2 in a nucleon-structure model. In this model, the nucleon has an outer cloud of quark-antiquark condensed ground state, an inner shell of topological baryonic charge ($r \simeq 0.44F$) probed by the vector meson ω, and a central quark-bag ($r \simeq 0.2F$) containing valence quarks. We also predict $d\sigma/dt$ in the Coulomb-hadronic interference region. Large $|t|$ elastic scattering in this model arises from valence quark-quark scattering, which is taken to be due to the hard-pomeron (BFKL pomeron with next to leading order corrections). We present results of taking into account multiple hard-pomeron exchanges, i.e. unitarity corrections. Finally, we compare our prediction of pp elastic $d\sigma/dt$ at LHC with the predictions of various other models. Precise measurement of pp $d\sigma/dt$ at LHC by the TOTEM group in the $|t|$ region $0 - 5$ GeV^2 will be able to distinguish between these models.

High energy pp and $\bar{\text{p}}$p elastic scattering have been at the forefront of accelerator research since the early seventies with the advent of CERN Intersecting Storage Rings (ISR) and measurement of pp elastic differential cross section in the c.m. energy range $\sqrt{s} = 23 - 62$ GeV and momentum transfer range $|t| = 0.8 - 10$ GeV^2 [1]. This was followed by the Fermilab accelerator where pp elastic scattering was measured at c.m. energy $\sqrt{s} = 27.4$ GeV in a fixed target experiment at large momentum transfers: $|t| = 5.5 - 14$ GeV^2 [2]. Next came the CERN SPS Collider, where $\bar{\text{p}}$p elastic scattering was measured at c.m. energies 546 GeV and 630 GeV – a jump of one order of magnitude in c.m. energy from ISR [3–5]. The Fermilab Tevatron followed next where $\bar{\text{p}}$p elastic scattering was measured at c.m. energy 1.8 TeV, but in a rather small momentum transfer range: $|t| = 0 - 0.5$ GeV^2 [6, 7]. We are now at the threshold of a new period of accelerator research with the LHC starting up soon and with the planned measurement of pp elastic scattering by the TOTEM group at c.m. energy 14 TeV and momentum transfer range $|t| \simeq 0 - 10$ GeV^2 [8, 9].

My collaborators and I have been studying pp and $\bar{\text{p}}$p elastic scattering since late seventies. From our phenomenological investigation, we have arrived at two results: 1) a physical picture of the nucleon, 2) an effective field theory model underlying the physical picture [10]. The physical picture shows that the nucleon has an outer cloud, an inner shell of baryonic charge,

---

*speaker

and a central quark-bag containing the valence quarks (Fig. 1). The radius of the shell is about 0.44 F and that of the quark-bag is 0.2 F. The underlying field theory model turns out to be a gauged Gell–Mann–Levy linear σ-model with spontaneous breakdown of chiral symmetry and with a Wess–Zumino–Witten (WZW) anomalous action. The model attributes the outer nucleon cloud to a quark–antiquark condensed ground state analogous to the BCS ground state in superconductivity– an idea that was first proposed by Nambu and Jona-Lasinio. The WZW action indicates that the baryonic charge is geometrical or topological in nature, which is the basis of the Skyrmion model. The action further shows that the vector meson ω couples to this topological charge like a gauge boson, i.e. like an elementary vector meson. As a consequence, one nucleon probes the baryonic charge of the other via ω-exchange. In pp elastic scattering, in the small momentum transfer region, the outer cloud of one nucleon interacts with that of the other giving rise to diffraction scattering. As the momentum transfer increases, one nucleon probes the other at intermediate distances and the ω-exchange becomes dominant. At momentun transfers even larger, one nucleon scatters off the other via valence quark-quark scattering.

Our calculated pp elastic $d\sigma/dt$ at c.m. energy 14 TeV is shown in Fig. 2 by the solid line that includes all three processes: diffraction, ω-exchange, and qq scattering. The dotted curve shows $d\sigma/dt$ due to diffraction only. We see that diffraction dominates in the small $|t|$ region, but falls off rapidly. The dot-dashed curve shows $d\sigma/dt$ due to ω-exchange only and indicates that ω-exchange dominates in the $|t|$ region $1.5 - 3.5$ GeV^2. Beyond that, the valence quark-quark scattering takes over. The dashed curve for $|t| > 3.5$ GeV^2 represents $d\sigma/dt$ with single valence quark-quark scattering, whereas the solid curve represents $d\sigma/dt$ with all multiple valence quark-quark scattering.

Let us next examine how the three processes are described in our calculations [10]. Diffraction is described by using the impact parameter representation and a phenomenological profile function:
$$T_D(s,t) = i\,p\,W \int_0^\infty b\,db\ J_0(b\,q)\Gamma_D(s,b); \tag{1}$$
q is the momentum transfer ($q = \sqrt{|t|}$) and $\Gamma_D(s,b)$ is the diffraction profile function, which is related to the eikonal function $\chi_D(s,b)$: $\Gamma_D(s,b) = 1 - \exp(i\chi_D(s,b))$. We take $\Gamma_D(s,b)$ to be an even Fermi profile function:
$$\Gamma_D(s,b) = g(s)[\tfrac{1}{1+e^{(b-R)/a}} + \tfrac{1}{1+e^{-(b+R)/a}} - 1]. \tag{2}$$
The parameters R and a are energy dependent: $R = R_0 + R_1(\ln s - i\frac{\pi}{2})$, $a = a_0 + a_1(\ln s - i\frac{\pi}{2})$; $g(s)$ is a complex crossing even energy-dependent coupling strength.

The diffraction amplitude we obtain has the following asymptotic properties:

1. $\sigma_{\text{tot}}(s) \sim (a_0 + a_1 \ln s)^2$ (Froissart-Martin bound)
2. $\rho(s) \simeq \frac{\pi a_1}{a_0 + a_1 \ln s}$ (derivative dispersion relation)
3. $T_D(s,t) \sim i\ s\ \ln^2 s\ f(|t|\ \ln^2 s)$ (Auberson-Kinoshita-Martin scaling)
4. $T_D^{\bar{p}p}(s,t) = T_D^{pp}(s,t)$ (crossing even)

Incidentally, the profile function (2) has been used by Frankfurt et al. to estimate the absorptive effect of soft hadronic interactions (gap survival probability) in the central production of Higgs at LHC [11].

The ω-exchange amplitude in our model has the form

$$T_\omega(s,t) \sim \exp[i \, \chi_D(s,0)] \, s \, \frac{F^2(t)}{m_\omega^2 - t}. \tag{3}$$

where the factor s shows that ω is behaving like an elementary spin-1 boson. The two form factors indicate that ω is probing two baryonic charge distributions – one for each nucleon. The factor $\exp[i \, \chi_D(s,0)]$ represents the absorptive effect due to soft hadronic interactions.

We view large $|t|$ elastic scattering as a hard collision of a valence quark from one proton with a valence quark from the other proton (Fig. 3). Since this process involves high energy quark-quark scattering at large momentum transfer, one would expect that it should be described by perturbative QCD. In fact, in perturbative QCD, the two quarks would interact via BFKL pomeron, that is, reggeized gluon ladders with rungs of gluons that lead to a fixed branch point in the angular momentum plane at $\alpha_{\text{BFKL}} = 1 + \omega$. The value of ω in next to leading order lies in the range $0.13 - 0.18$ as argued by Brodsky et al. [12]. We refer to the BFKL pomeron with next to leading order corrections included as the "hard-pomeron". In our calculations, we approximate the hard-pomeron by a fixed pole and take the corresponding qq amplitude as [13]

$$\hat{T}_1(\hat{s},t) = i \, \gamma_{\text{qq}} \, \hat{s} \, \left(\hat{s} \, e^{-i\frac{\pi}{2}} \right)^\omega \frac{1}{|t| + r_0^{-2}}, \tag{4}$$

where $\hat{s}$ is the square of the c.m. energy of qq scattering.

Our pp elastic $d\sigma/dt$ calculation at 14 TeV reported earlier [10,13] included only a single hard-pomeron exchange in qq scattering. However, Eq. (4) shows that the hard-pomeron predicts a qq asymptotic total cross section $\hat{\sigma}_{\text{tot}}(\hat{s}) \propto \hat{s}^\omega$, i.e. $\hat{\sigma}_{\text{tot}}(\hat{s})$ grows like a power of $\hat{s}$ and therefore violates unitarity and the Froissart-Martin bound. To restore unitarity in the qq channel, we use the eikonal representation and write the full qq scattering amplitude as

$$\hat{T}(\hat{s},t) = i\hat{p}\hat{W} \int_0^\infty b \, db \, J_0(bq) \left[1 - e^{i\hat{\chi}(\hat{s},b)} \right]. \tag{5}$$

Taking $\hat{T}_1(\hat{s},t)$ in Eq. (4) as the Born or single-scattering amplitude, we obtain by inverting it

$$\hat{\chi}(\hat{s},b) = 2 \, i \, \gamma_{\text{qq}} \, \left(\hat{s} \, e^{-i\frac{\pi}{2}} \right)^\omega \, K_0(\tfrac{b}{r_0}). \tag{6}$$

Expanding the exponential in (5), we get

$$\hat{T}(\hat{s},t) = -i \, \hat{p} \, \hat{W} \, \int_0^\infty b \, db \, J_0(bq) \left[i \, \hat{\chi} - \frac{\hat{\chi}^2}{2!} - i \, \frac{\hat{\chi}^3}{3!} + \frac{\hat{\chi}^4}{4!} + ... \right]. \tag{7}$$

The nth term in the series is

$$\hat{T}_n(\hat{s},t) = -i \, \frac{(-1)^n \, 2^{n-1}}{n!} \, \gamma_{\text{qq}}^n \, \hat{s} \, \left(\hat{s} \, e^{-i\frac{\pi}{2}} \right)^{n\omega} \int_0^\infty b \, db \, J_0(bq) \, K_0^n \left(\frac{b}{r_0} \right). \tag{8}$$

Now, $\hat{s} \simeq xx's$, where x and x' are the longitudinal momentum fractions of the protons carried by the valence quarks (Fig. 3). This leads to the following pp elastic amplitude due to qq scattering:

$$T_{\text{qq}}(s,t) = \hat{T}_1(s,t) \, \mathcal{F}_1^2(q_\perp) + \hat{T}_2(s,t) \, \mathcal{F}_2^2(q_\perp) + ... + \hat{T}_n(s,t) \, \mathcal{F}_n^2(q_\perp); \tag{9}$$

$\mathcal{F}_1$, $\mathcal{F}_2$,... $\mathcal{F}_n$ are the structure factors that take into account momentum distributions of the valence quarks inside the proton. Our earlier calculation kept only the first term in Eq. (9). Fig. 2 shows that the effect of multiple hard-pomeron exchange in pp scattering is to decrease $d\sigma/dt$ at large $|t|$ compared to $d\sigma/dt$ due to single hard-pomeron exchange (dashed line in Fig. 2). For $|t| < 3.5$ GeV^2, there is little effect due to multiple scattering, i.e. unitarization.

Results of some of our quantitative calculations are shown in Figs. 4–7. The solid curve in Fig. 4 represents our calculated total cross section as a function of $\sqrt{s}$. Dotted curves represent the error band given by Cudell et al. [14]. In Fig. 5, solid and dashed curves represent our calculated $\rho_{\bar{p}p}$ and ρ_{pp} respectively ($\rho = \text{Re } T(s,0)/\text{Im } T(s,0)$). Dotted curves, as before, represent the error band given by Cudell et al. At $\sqrt{s}$=14 TeV, our values of σ_{tot} and ρ_{pp} are

109.4 mb and 0.12 respectively. Fig. 6 shows our calculated $\mathrm{d}\sigma/\mathrm{d}t$ for $\bar{\mathrm{p}}\mathrm{p}$ elastic scattering at $\sqrt{s}$ = 541 GeV in the Coulomb–hadronic interference region using the Kundrát–Lokajíček formulation (upper curve) and West–Yennie formulation (lower curve). Experimental data are from Augier et al. [15]. Fig. 7 shows our predicted $\mathrm{d}\sigma/\mathrm{d}t$ for pp elastic scattering at $\sqrt{s}$ = 14 TeV in the Coulomb–hadronic interference region. Finally, in Fig. 8, we compare our predicted pp elastic $\mathrm{d}\sigma/\mathrm{d}t$ at LHC with the predictions of other models proposed by various groups: Avila et al. [16], Block et al. [17], Bourrely et al. [18], Desgrolard et al. [19], and Petrov et al. (three pomeron) [20].

Conclusions

1. Precision measurement of pp elastic $\mathrm{d}\sigma/\mathrm{d}t$ at LHC by the TOTEM group in the region $|t| = 0$ – 5 GeV^2 will be able to distinguish between various proposed models (see Fig. 8).

2. In our nucleon-structure model, the qualitative saturation of the Froissart-Martin bound is due to soft hadronic interactions.

3. Large $|t|$ elastic scattering in our model is due to valence quark-quark scattering. This has been described by us as due to the exchange of a hard-pomeron (BFKL pomeron plus next to leading order corrections).

4. Unitarization of the hard-pomeron exchange leads to a decrease of $\mathrm{d}\sigma/\mathrm{d}t$ at large $|t|$, but has little effect on forward $\mathrm{d}\sigma/\mathrm{d}t$.

5. The nucleon structure that we find embodies salient features of many leading models– such as Nambu-Jona-Lasinio model, Skyrmion model, nonlinear σ-model, chiral-bag model– but, at the end, it presents a unique description of the nucleon.

References

[1] E. Nagy *et al.*, Nucl. Phys. B **150**, 221 (1979).

[2] W. Faissler *et al.*, Phys. Rev. D **23**, 33 (1981).

[3] UA4 Collaboration, M. Bozzo *et al.*, Phys. Lett. B **147**, 385 (1984).

[4] UA4 Collaboration, M. Bozzo *et al.*, Phys. Lett. B **155**, 197 (1985).

[5] D. Bernard *et al.*, Phys. Lett. B **171**, 142 (1986).

[6] N. Amos *et al.*, Phys. Lett. B **247**, 127 (1990).

[7] F. Abe *et al.*, Phys. Rev. D **50**, 5518 (1994).

[8] TOTEM Collaboration, Technical Design Report CERN-LHCC-2004-002.

[9] TOTEM Collaboration, CERN-LHCC-2007-013/G130.

[10] M. M. Islam, R. J. Luddy, and A. V. Prokudin, Int. J. Mod. Phys. A **21**, 1 (2006).

[11] L. Frankfurt, M. Strickman, C. Weiss, and M. Zhalov, Czech. J. Phys. **55**, B675 (2005).

[12] S. Brodsky, V. S. Fadin, V. T. Kim, L. N. Lipatov, and G. B. Pivovarov, JETP Lett. **70**, 155 (1999).

[13] M. M. Islam, R. J. Luddy, and A. V. Prokudin, Phys. Lett. B **605**, 115 (2005).

[14] J. R. Cudell *et al.*, Phys. Rev. Lett. **89**, 201801 (2002).

[15] C. Augier *et al.*, Phys. Lett. B **316**, 498 (1993).

[16] R. F. Avila, S. D. Campos, M. J. Menon, and J. Montanha, Eur.Phys.J. C **47**, 171 (2006).

[17] M. M. Block, E. M. Gregores, F. Halzen, and G. Pancheri, Phys. Rev. D **60**, 054024 (1999).

[18] C. Bourrely, J. Soffer, and T. T. Wu, Eur. Phys. J. C **28**, 97 (2003).

[19] P. Desgrolard, M. Giffon, E. Martynov, and E. Predazzi, Eur. Phys. J. C **16**, 499 (2000).
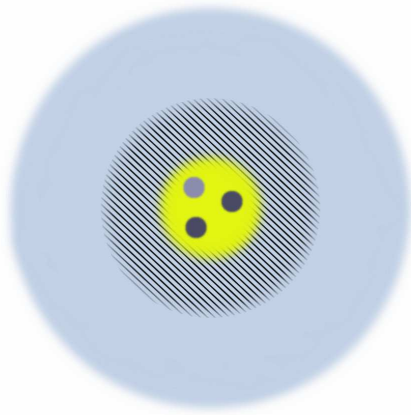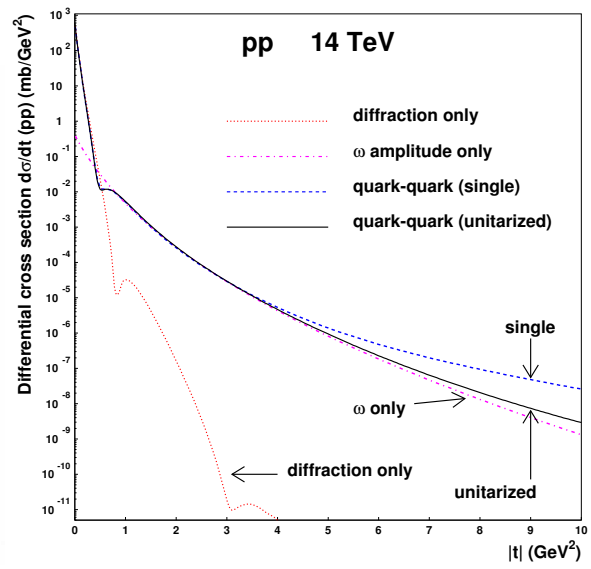
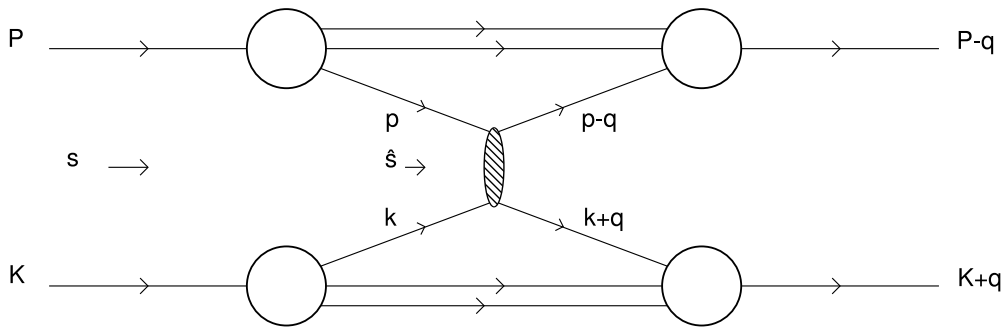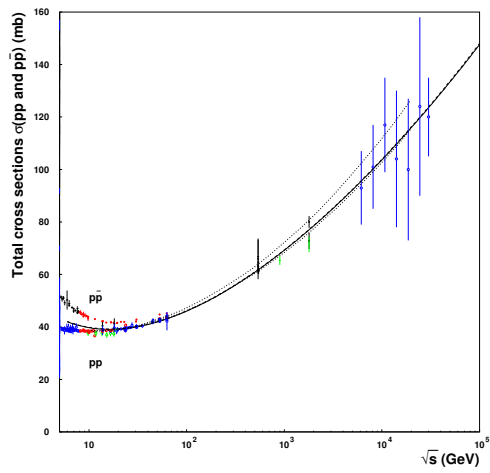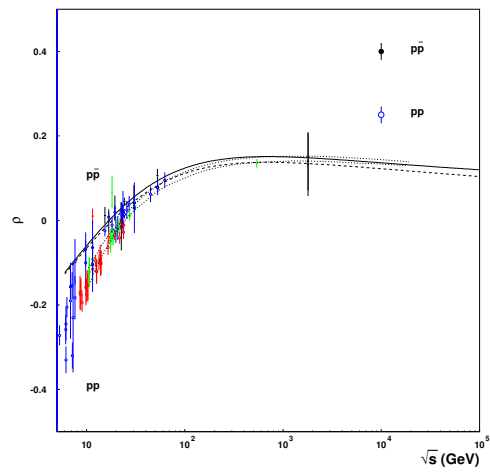[20] V. Petrov, E. Predazzi, and A. V. Prokudin, Eur. Phys. J. C **28**, 525 (2003).

Fig. 1

Fig. 2

Fig. 3

Fig. 4

Fig. 5

Fig. 6

Fig. 7

Fig. 8